Available online at www.sciencedirect.com
SCIENCE DIRECT®
Solid State Sciences 7 (2005) 1333–1343
Solid State Sciences
www.elsevier.com/locate/ssscie

Chemical interaction between $Ba_2YCu_3O_{6+x}$ and CeO_2 at $p_{O_2} = 100$ Pa

W. Wong-Ng [a,*], Z. Yang [a], L.P. Cook [a], Q. Huang [a], J.A. Kaduk [b], J. Frank [a]

[a] *Materials Science and Engineering Laboratory, National Institute of Standards and Technology, Gaithersburg, MD 20899, USA*
[b] *BP-Amoco Research, Naperville, IL 60566, USA*

Received 29 April 2005; received in revised form 5 July 2005; accepted 8 July 2005

Available online 25 August 2005

Abstract

Chemical interaction between the $Ba_2YCu_3O_{6+x}$ superconductor and the CeO_2 buffer layers employed in coated conductor architectures has been modeled experimentally by investigating phase equilibria on the $Ba_2YCu_3O_{6+x}$–CeO_2 join at $p_{O_2} = 100$ Pa. This join is actually a non-binary join within the BaO–Y_2O_3–CeO_2–CuO_x quaternary system. At an approximate mole ratio of $Ba_2YCu_3O_{6+x} : CeO_2 = 40 : 60$, a phase boundary was found to separate two four-phase regions. At the $Ba_2YCu_3O_{6+x}$-rich side of the join, the four-phase region consists of $Ba_2YCu_3O_{6+x}$, $Ba(Ce_{1-z}Y_z)O_{3-x}$, BaY_2CuO_5, and Cu_2O; at the CeO_2 rich side, the four phases were determined to be $Ba(Ce_{1-z}Y_z)O_{3-x}$, BaY_2CuO_5, Cu_2O and CeO_2. At 810 °C and $p_{O_2} = 100$ Pa, there appears to be negligible solid solution formation of the types $Y_{1-z}Ce_zO_{3-x}$ and $Ce_{1-z}Y_zO_{2-x}$. The minimum melting temperature along the $Ba_2YCu_3O_{6+x}$–CeO_2 join was determined to be ≈ 860 °C. As part of this study, phase diagrams of the subsystems CeO_2–Y_2O_3–CuO_x, BaO–CeO_2–CuO_x, and BaO–Y_2O_3–CeO_2 were also determined at 810 °C under 100 Pa p_{O_2}. The Y_2O_3–CeO_2–CuO_x diagram does not contain ternary phases and shows a tie-line from Y_2O_3 to the binary phase $Y_2Cu_2O_{5-x}$. Similarly, the BaO–CeO_2–CuO_x diagram contains no ternary phases, but has four tie-lines originating from $BaCeO_3$ to Ba_2CuO_{3+x}, $BaCuO_{2+x}$, $BaCu_2O_{2+x}$ and CuO_x. The BaO–Y_2O_3–CeO_2 system contains one ternary phase, the solid solution $Ba(Ce_{1-z}Y_z)O_{3-x}$ ($0 \leqslant z \leqslant 0.13$), which crystallizes with the orthorhombic space group *Pmcn* (No. 62). Neutron Rietveld refinement of $Ba(Ce_{0.94}Y_{0.06})O_{2.84}$ [$Ba(Ce^{3+}{}_{0.26}Ce^{4+}{}_{0.68}Y_{0.06})O_{2.84}$] gives lattice parameters of $a = 8.7817(4)$ Å, $b = 6.2360(4)$ Å, $c = 6.2190(3)$ Å, $V = 340.57$ Å^3, $Z = 4$. The structure consists of distorted corner-shared $(Ce,Y)O_6$ octahedra that are tilted with respect to each other. Ba was found to have 9 nearest neighbors (distances < 3.5 Å). Reference X-ray patterns of $Ba(Ce_{0.90}Y_{0.10})O_{2.95}$ and $Ba(Ce_{0.87}Y_{0.13})O_{2.93}$ were submitted to be included in the Powder Diffraction File (PDF).
Published by Elsevier SAS.

Keywords: Reaction of $Ba_2YCu_3O_{6+x}$ with CeO_2; BaO–Y_2O_3–CeO_2–CuO_x; BaO–Y_2O_3–CeO_2; Y_2O_3–CeO_2–CuO_x; BaO–CeO_2–CuO_x; $Ba(Ce_{0.94}Y_{0.06})O_{2.84}$ structure

1. Introduction

Electricity outages and energy shortages have become increasingly common features of the global energy picture, with obvious needs for improvement in the electrical distribution grid and for more efficient utilization of energy sources. High-temperature superconductors have demonstrated potential for meeting these needs, leading to accelerated effort within the high T_c community on the research and development of coated conductors for wire/tape applications. With the advent of coated conductor technologies [1–9], there has been a renewal of interest in $Ba_2YCu_3O_x$ (Y-213) and $Ba_2RCu_3O_x$ (R-213) (R = lanthanides) as the principal superconducting materials. Relative to (Bi,Pb)-2223 (Bi(Pb) : Sr : Ca : Cu : O = 2 : 2 : 2 : 3) superconductors, which typically are processed using the powder-in-tube method [10–14], Y-213 and R-213 can be readily deposited on flexible metallic tapes, and the resulting materials show much improved current-carrying capability under applied magnetic field. The three state-of-the-art technologies to produce biaxially-textured substrates for coated conductor applications are commonly known as Ion Beam Assisted Deposition (IBAD) [1,2], Rolling Assisted Bi-axially Textured

* Corresponding author.
E-mail address: winnie.wong-ng@nist.gov (W. Wong-Ng).

1293-2558/$ – see front matter Published by Elsevier SAS.
doi:10.1016/j.solidstatesciences.2005.07.002

Substrate (RABiTS) [3–7], and Inclined Substrate Deposition (ISD) [8,9]. The issues of cost and performance are closely linked to the optimized processing of these materials.

The IBAD, RABiTS, and ISD methods all involve deposition of Y-213 or R-213 film on biaxially-textured buffered substrate. An example of the typical architecture of a RABiTS film involves the following layers deposited on the metallic substrate: seed layer, barrier layer, lower cap layer, superconductor layer, and another cap layer on the superconductor [15]. The function of a biaxially grown substrate is to guide the growth of epitaxial oxide buffer (seed, barrier, lower cap) layers, and Y-213 layers. The seed layer provides a thin epitaxial layer for protecting the substrate from oxidation during deposition of barrier layer. The barrier layer is a thick epitaxial layer for providing a physical/chemical barrier to substrate oxidation and substrate reaction with the superconductor layer. Ideally, the lower cap layer provides additional protection for the superconductor film from chemical reaction with underlying layers, while transmitting the textural information on the crystallographic alignment. Examples of cap layers immediately below the Y-213 film currently being investigated for the coated conductor process include CeO_2, $LaMnO_3$, $SrTiO_3$, Gd_3NbO_7, and $SrRuO_3$. The two most extensively used materials have been CeO_2 and $SrTiO_3$; studies of interfacial reactions between $Ba_2YCu_3O_{6+x}$ and CeO_2 [16,17], and between $Ba_2YCu_3O_{6+x}$ and $SrTiO_3$ [16,18,19] using the transmission electron diffraction (TEM) technique and other methods have been reported.

For a given combination of buffer layers that has been found to promote epitaxial growth of $Ba_2YCu_3O_{6+x}$, there may be unavoidable reactions at the interface between layers. Understanding of interfacial reactions of Y-213 phase with the buffer layers will provide information about how to avoid and/or control the formation of second phases. Phase equilibrium data will compliment the results of TEM analysis of coated conductor interfaces. This paper describes the phase equilibria of the multi-component systems representing the interaction of $Ba_2YCu_3O_{6+x}$ with the most effective coated conductor buffer material, CeO_2. Study of the non-binary join $Ba_2YCu_3O_{6+x}$–CeO_2 within the BaO–Y_2O_3–CeO_2–CuO_x quaternary system, as well as studies of the subsolidus diagrams of the ternary subsystems, CeO_2–Y_2O_3–CuO_x, BaO–CeO_2–CuO_x, and BaO–Y_2O_3–CeO_2, and the structure of the $Ba(Ce_{1-z}Y_z)O_{3-x}$ phase by neutron diffraction, will be reported. In order to determine the lowest temperature at which melt could occur at the $Ba_2YCu_3O_{6+x}$–CeO_2 interface, we completed differential thermal analysis (DTA) and quenching experiments [20]. Our experiments were completed under atmospherically-controlled conditions, which has allowed us to construct a partial liquidus diagram for the non-binary join $Ba_2YCu_3O_{6+x}$–CeO_2 at $p_{O_2} = 100$ Pa.

Powder X-ray diffraction is a technique of primary importance for phase characterization, and the extensive coverage and accurate reference diffraction patterns of the perovskite-related phases found in the Powder Diffraction File (PDF) [21] are essential for the materials research community. Currently powder patterns of $Ba(Ce_{1-z}Y_z)O_{3-x}$ are not in the PDF; a second goal of this investigation was therefore to produce quality diffraction patterns of these materials, refined using the X-ray Rietveld technique [22–24], and suitable for inclusion in the PDF.

2. Experimental[1]

2.1. Sample preparation

2.1.1. Preparation of BaO

The BaO starting material was produced from $BaCO_3$ (99.99% purity, metals basis) by vacuum calcination in a specially designed vertical tube furnace. An MgO crucible containing ≈ 15 g of $BaCO_3$ was suspended in the hot zone of the furnace, and the furnace was evacuated to a pressure of ≈ 10 µm Hg or less by a high capacity mechanical pump. The following heating schedule was used: room temperature to 1300 °C in 20 h; isothermal at 1300 °C for 10 h; 1300 °C to room temperature in 20 h. During vacuum calcination the pressure typically increased to ≈ 200 µm Hg as CO_2 was evolved, and then rapidly returned to ≈ 10 µm Hg or less as the decomposition of the $BaCO_3$ was completed. After cooling, the BaO was lowered through an interlock into a transfer vessel. It was then transported to an Ar-filled glove-box continually purged with a recirculating purifier, which removed atmospheric contaminants from the Ar to < 1 ppm by volume. Characterization by X-ray powder diffraction showed only the characteristic peaks for BaO.

2.1.2. Preparation of samples in the $Ba_2YCu_3O_{6+x}$–CeO_2 system

A master batch of the superconductor phase $Ba_2YCu_3O_{6+x}$ was prepared using BaO, Y_2O_3 and CuO under purified air. Samples were weighed out, well mixed and calcined in an atmospherically controlled high temperature furnace first at 850 °C, then at 930 °C repeatedly with intermediate grindings for about two weeks. Thirteen samples with different ratios of $Ba_2YCu_3O_{6+x}$: CeO_2 were then prepared using the master $Ba_2YCu_3O_{6+x}$ batch (5 : 95, 10 : 90, 20 : 80, 30 : 70, 35 : 65, 40 : 60, 45 : 55, 50 : 50, 60 : 40, 70 : 30, 80 : 20, 90 : 10, and 95 : 5). The processes of sample weighing, sample homogenization and pellet-pressing were performed inside a glove-box. Pelletized samples were placed inside individual MgO crucibles for annealing in a horizontal box-type controlled-atmosphere furnace. Transfer from

[1] Certain trade names and company products are mentioned in the text or identified in illustrations in order to adequately specify the experimental procedure and equipment used. In no case does such identification imply recommendation or endorsement by National Institute of Standards and Technology.

the glove-box to the box furnace and vice versa was achieved via a second transfer vessel and an interlock system attached to the furnace.

2.1.3. Determination of the ternary phase diagrams

Thirty-four compositions for the $BaO–CeO_2–Y_2O_3$ system (Table 1), nine for the $CeO_2–Y_2O_3–CuO_x$ system (Table 2), and ten for the $BaO–CeO_2–CuO_x$ system (Table 3) were prepared using the solid state sintering method. Stoichiometric amounts of BaO, CeO_2, CuO and Y_2O_3 (99.99% purity, metals basis) were first weighed inside a dry box according to the proper mole ratio, and were then mixed and pressed into pellets, followed by annealing in a controlled-atmosphere furnace. Sample transfer was accomplished by using an air-tight vessel. During the annealings, the oxygen pressure of Ar/O_2 mixtures was controlled using a mass flow meter and monitored at both the inlet and outlet of the furnace using a zirconia oxygen sensor. Samples were studied under two conditions: under ambient conditions (with the presence of CO_2) and under atmospherically-controlled conditions at 810 °C with $p_{O_2} = 100$ Pa (0.1% O_2 by volume fraction) (in the absence of CO_2). Intermediate grindings and pelletizings took place until no further changes were detected in the powder X-ray diffraction patterns. Samples were processed for about 3 weeks each. Differential thermal analysis (DTA) was used to study the melting of the samples.

Table 1
Compositions prepared in the $BaO–Y_2O_3–CeO_2$ system

BaO	$\frac{1}{2}Y_2O_3$	CeO_2	BaO	$\frac{1}{2}Y_2O_3$	CeO_2
–	10	90	–	20	80
50	15	35	50	20	30
50	25	25	50	30	20
50	35	15	50	40	10
50	45	5	60	5	35
9.5	7.5	8.5	40	5	55
15	20	65	25	40	35
35	50	15	25	–	75
20	–	70	60	25	15
–	10	90	–	20	80
–	30	70	–	40	60
–	50	50	30	50	20
50	10	40	32	13	55
35	35	30	70	3	27
25	10	65	–	2	98
–	5	95	–	2.5	97.5
36	54	10	70	15	15

Table 2
Compositions prepared in the $BaO–CeO_2–CuO_x$ system

BaO	CeO_2	CuO_x	BaO	CeO_2	CuO_x
25	50	25	40	5	55
25	65	10	50	5	45
50	25	25	65	25	10
10	45	45	33.33	16.67	50
25	5	70	60	10	30

Table 3
Compositions prepared in the $CeO_2–Y_2O_3–CuO_x$ system

CeO_2	$\frac{1}{2}Y_2O_3$	CuO_x	CeO_2	$\frac{1}{2}Y_2O_3$	CuO_x
40	45	15	2.5	47.5	50
40	15	45	4.5	45.5	50
2	70	28	7.5	42.5	50
2	25	73	10.0	40.0	50
–	50	50	12.5	37.5	50

2.2. X-ray diffraction

X-ray powder diffraction was used to identify the phases synthesized, to confirm phase purity, and to determine phase relationships. All X-ray patterns were measured using a hermetic cell designed for air-sensitive materials [25]. A computer-controlled automated diffractometer equipped with a θ-compensation slit and CuK_α radiation was operated at 45 kV and 40 mA. The radiation was detected by a scintillation counter and a solid-state amplifier. The Siemens software package and the reference X-ray diffraction patterns of the Powder Diffraction File (PDF) [21] were used for performing phase identification.

Two reference X-ray patterns for $Ba(Ce_{1-z}Y_z)O_{3-x}$ were measured with a Rietveld pattern decomposition technique [23]. These patterns represent ideal specimen patterns. They are corrected for systematic errors both in d-spacing and intensity. The reported peak positions are calculated from the refined lattice parameters, as this represents the best measure of the true positions. For peaks resolved at the instrument resolution function, the individual peak positions are reported. For overlapping peaks, the intensity-weighted average peak position is reported with multiple indices. For marginally-resolved peaks, individual peaks are reported to more accurately simulate the visual appearance of the pattern.

2.3. Neutron diffraction

One selected sample within the $Ba(Ce_{1-z}Y_z)O_{3-x}$ solid solution was studied using neutron diffraction. Neutron diffraction data were collected with the 32 detector BT-1 diffractometer at the NIST Center for Neutron Research using a Cu(311) monochromator ($\lambda = 1.5396(1)$ Å). Samples were loaded in a 6 mm diameter well-sealed vanadium container. Measurements were made under ambient conditions. A 6 gm sample was prepared for this study.

The structural refinement was performed by using the GSAS software suite [22–24]. The structure of $BaCeO_3$ was employed as the initial model for the refinements. The neutron scattering length of the elements Ba/Ce/Y/O are 0.52/0.484/0.775/0.581, respectively. The parameters refined included scale factor, background function (high order polynomials), profile parameters (U, V, W), asymmetry coefficient, lattice parameters, atomic coordinates, and isotropic temperature factors.

2.4. Differential thermal analysis

Simultaneous differential thermal analysis and thermogravimetric analysis (DTA/TGA) were used to study thermal events. Most experiments utilized primarily the DTA signal; the TGA signal was useful primarily in following oxygen gain/loss associated with the CuO_x component. DTA/TGA experiments were performed using an electronically upgraded Mettler TA-1 system fitted with an Anatech digital control and readout system. The DTA/TGA apparatus was calibrated against the α/β quartz transition (571 °C) and the melting point of NaCl (801 °C), and temperatures reported in this study have a standard uncertainty of ±5 °C. Event temperatures were determined as the intersection of the baseline with the extrapolated linear portion of the rising DTA peak. Oxygen partial pressure during DTA/TGA was controlled using an analyzed Ar/O_2 mixtures. During the experiments, gas was continuously flowed through the sample region at a rate of 150 ml/min, and the oxygen pressure at the outlet of the DTA/TGA system was periodically checked with a zirconia sensor.

3. Results and discussion

In the following, a description of the interaction between $Ba_2YCu_3O_{6+x}$ and CeO_2 will be discussed in terms of a four-component diagram, $BaO–Y_2O_3–CeO_2–CuO_x$, and a partial diagram of the non-binary join $Ba_2YCu_3O_{6+x}–CeO_2$. In addition, subsolidus phase relations of the limiting binary systems such as $BaO–CeO_2$, $CeO_2–CuO_x$, $BaO–CuO_x$, $BaO–Y_2O_3$, $Y_2O_3–CuO_x$, and $Y_2O_3–CeO_2$, and the ternary systems such as $BaO–CeO_2–CuO_x$, $BaO–CeO_2–Y_2O_3$, and $CeO_2–Y_2O_3–CuO_x$ will be described.

3.1. Chemical interaction between $Ba_2YCu_3O_{6+x}$ and CeO_2

Fig. 1 illustrates the equilibria along the $Ba_2YCu_3O_{6+x}–CeO_2$ join in the context of the $BaO–\frac{1}{2}Y_2O_3–CuO_x–CeO_2$ framework. It is seen clearly that two tetrahedral volumes (4-phase regions) corresponding to $Ba_2YCu_3O_{6+x}–BaCeO_3–BaY_2CuO_5–Cu_2O$ and $BaCeO_3–BaY_2CuO_5–Cu_2O–CeO_2$ are mutually consistent and do not overlap. These two tetrahedra share a common plane defined by BaY_2CuO_5 (the so-called green phase), Cu_2O and CeO_2. In other words, as a composition vector passes through the two tetrahedra, only three phases are observed at the boundary. This phase boundary exists at the mole ratio of $Ba_2YCu_3O_{6+x} : CeO_2 = 40 : 60$. On the $Ba_2YCu_3O_{6+x}$-rich side, the four phases possible as a result of chemical interaction were found to be $Ba_2YCu_3O_{6+x}$, $Ba(Ce_{1-z}Y_z)O_{3-x}$, BaY_2CuO_5, and Cu_2O; whereas at the CeO_2 rich side, the four phases are $Ba(Ce_{1-z}Y_z)O_{3-x}$, BaY_2CuO_5, CeO_2 and Cu_2O. Apparently Cu_2O is more stable than CuO at $p_{O_2} = 100$ Pa, in agreement with calculated CuO/Cu_2O equilibria [26].

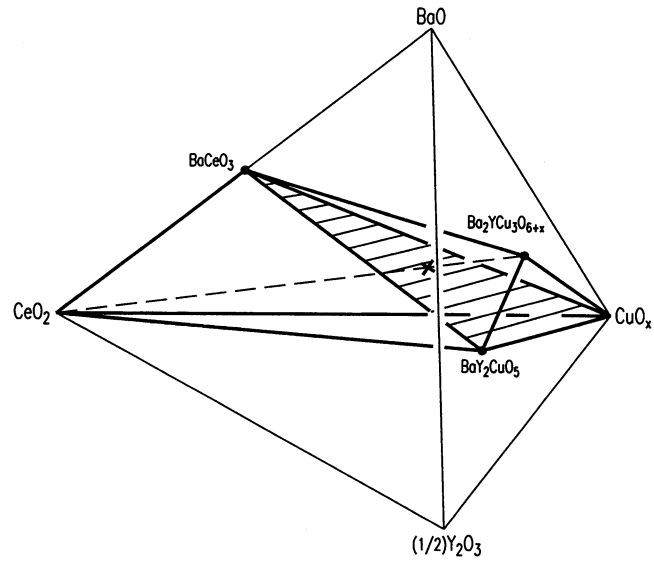

Fig. 1. The $BaO–Y_2O_3–CuO_x–CeO_2$ tetrahedron showing the two sub-volumes $Ba_2YCu_3O_{6+x}–BaCeO_3–BaY_2CuO_5–Cu_2O$ and $BaCeO_3–BaY_2CuO_5–Cu_2O–CeO_2$ within which the compositions of the $Ba_2YCu_3O_{6+x}–CeO_2$ join lie. The Y-doped $BaCeO_3$ phase is actually a solid solution of the formula $Ba(Ce_{1-z}Y_z)O_{3-x}$.

The $Ba(Ce_{1-z}Y_z)O_{3-x}$ phase is a solid solution, although it is represented as a point compound on Fig. 1 as an approximation. At 810 °C with $p_{O_2} = 100$ Pa, the extent of solid solution is rather limited ($Ba(Ce_{1-z}Y_z)O_{3-x}$, with $0 \leqslant z \leqslant 0.13$). The structure of $Ba(Ce_{1-z}Y_z)O_{3-x}$ is of the perovskite type, as discussed below.

Cerium is known to possess various oxidation states (+2, +3 and +4), therefore CeO_{2-x} undergoes a complex oxidation/reduction chemistry under different oxygen partial pressures. Numerous reports concerning the non-stoichiometry of CeO_x [27,28], and the co-existence of CeO_2 and Ce_2O_3 have been published [29–31]. Apparently CeO_2 converts to Ce_2O_3 at higher temperature before melting (a range reported to be between 1973 to 2600 °C). Under the conditions of the present study, CeO_2 is the only stable form of cerium oxide. Fig. 2 illustrates an approximate partial liquidus diagram of the nonbinary join $Ba_2YCu_3O_{6+x}–CeO_2$ constructed under $p_{O_2} = 100$ Pa. Since the melt temperature near the CeO_2-rich side is too high to determine with our DTA (no thermal event was observed below 1400 °C), the upper bound of the liquidus is represented as broken lines. The initial melt temperature of the thirteen compositions can be categorized into two groups. Compositions of Y-213 : CeO_2 ratio of 90 : 10, 80 : 20, 70 : 30, 60 : 40, and 45 : 55 gave an average melting temperature of 860 °C. Compositions with Y-213 : CeO_2 ratio of 40 : 60, 30 : 70, 20 : 80 and 10 : 90 gave an average melting temperature of 959 °C. Therefore the minimum melting temperature of this nonbinary join occurs near the $Ba_2YCu_3O_{6+x}$ side, and is estimated to take place according to the following reaction,

$$Ba_2YCu_3O_{6+x} + Cu_2O + BaY_2CuO_5 + Ba(Ce_{1-z}Y_z)O_{3-x} \rightarrow L \quad (\approx 860\,°C).$$

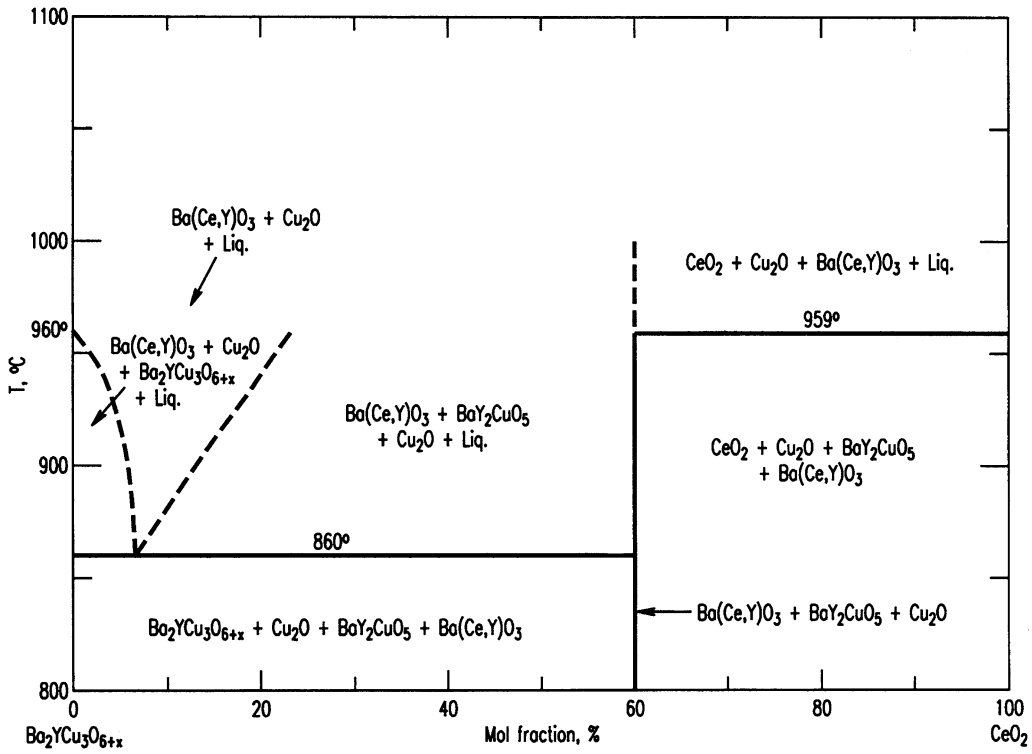

Fig. 2. A schematic phase diagram of the $Ba_2YCu_3O_{6+x}$–CeO_2 non-binary join ($p_{O_2} = 100$ Pa) showing the melting temperatures of various regions in the diagram. The Y-doped $BaCeO_3$ phase is actually a solid solution of the formula $Ba(Ce_{1-z}Y_z)O_{3-x}$.

The next-lowest melting temperature event occurred at $\approx 959\,°C$ (near the CeO_2 side). The melting of Y-213 decreased from the reported value of 1015 to 1020 °C in air [32] to 969.2 °C under $p_{O_2} = 100$ Pa. On the basis of these observations, since coated conductor processing takes place below 800 °C, the interaction of $Ba_2YCu_3O_{6+x}$ with CeO_2 will not cause melting during processing, unless extraordinary surface energy effects are operative.

3.2. *Phase diagrams of the BaO–Y_2O_3–CeO_2–CuO_x subsystems*

Three ternary subsystems within the quaternary system, BaO–Y_2O_3–CeO_2–CuO_x, have not been reported before: BaO–Y_2O_3–CeO_2, CeO_2–Y_2O_3–CuO_x, and BaO–CeO_2–CuO. The following summarizes the crystal chemistry and phase equilibria of these systems and the pertinent binary systems. Furthermore, the phase diagram of the BaO–Y_2O_3–CuO_x system that has been determined in this laboratory previously [33] will also be reviewed briefly in this paper.

3.2.1. *Binary systems*

BaO–CeO_2. In the BaO–CeO_2 system, only one binary compound $BaCeO_3$ is found [34]. An eutectic is located at $1440 \pm 5\,°C$ and (46 ± 0.5) mole fraction % of CeO_2. We confirmed that $BaCeO_3$ is the only binary phase in this system.

CeO_2–CuO_x. From the report by Pieczulewski et al. [35], there is no binary compound in the CeO_2–CuO system. We have confirmed this finding in our experiments conducted under $p_{O_2} = 100$ Pa.

BaO–CuO_x. A review of the compounds in the BaO–CuO_x was given by Wong-Ng and Cook [36]. Under $p_{O_2} = 100$ Pa [33,37,38], the phases formed are Ba_2CuO_{3+x}, $BaCuO_{2+x}$, and $BaCu_2O_{2+x}$. The CuO_x phase appears in the reduced Cu_2O form [26].

Y_2O_3–CuO_x. Only one binary phase exists in this system, namely, $Y_2Cu_2O_5$ [39–41]. The $YCuO_2$ phase was reported to form under much more reduced conditions [42,43].

BaO–Y_2O_3. When the samples of this system are prepared under atmospherically-controlled conditions, namely, in the absence of carbonate, only two compounds exist (Ba_2YO_4 and $Ba_3Y_4O_9$) [33,44–47]. However, in the presence of carbonate (or air), two additional oxycarbonates with higher barium content also exist: $Ba_4Y_2O_7{\cdot}xCO_2$, and $Ba_2Y_2O_5{\cdot}xCO_2$ [44].

Y_2O_3–CeO_2. Crystal chemistry and phase equilibria in this system have been studied extensively [48–53]. It has been reported that the solubility of yttrium in ceria varies depending on the dopant concentration (from a mole fraction of 0.05 to 40%) [48,49]. For example, the solubility was found to be about 20.5 mole fraction % at 1500 °C [50]. However, under reduced conditions at 810 °C, no significant solid solution of either end-member was found. Furthermore, no binary compound forms in the Y_2O_3–CeO_2 system.

3.2.2. Ternary systems

$BaO–CeO_2–Y_2O_3$

(a) Subsolidus diagram. Figs. 3 and 4 give the subsolidus diagrams of the $BaO–Y_2O_3–CeO_2$ system that were determined using BaO and $BaCO_3$ as a starting component, respectively. These diagrams appear to be rather simple. Along the $BaO–Y_2O_3$ side, only two phases under carbonate-free condition were found, namely, BaY_2O_4 and $Ba_3Y_4O_9$; whereas under the ambient conditions where one end member is $BaCO_3$, four phases were determined instead. As mentioned above, in addition to BaY_2O_4 [54] and $Ba_3Y_4O_9$ [55], two additional phases are oxycarbonates, $Ba_2Y_2O_5{\cdot}xCO_2$ and $Ba_4Y_2O_7{\cdot}xCO_2$.

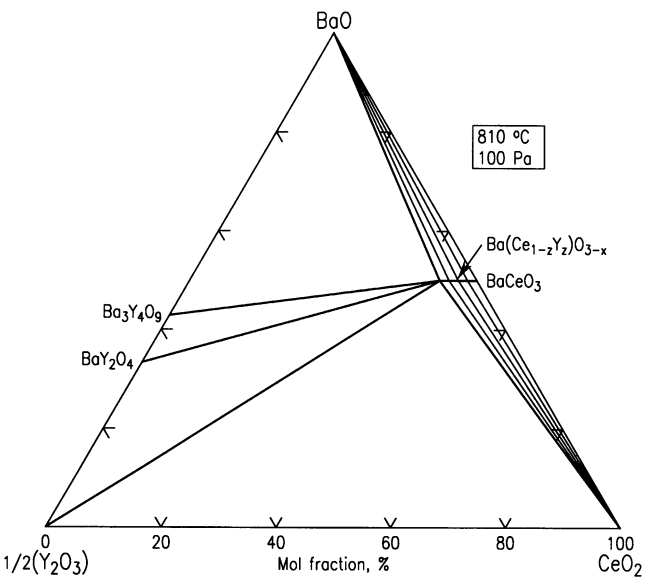

Fig. 3. Subsolidus diagram of the $BaO–Y_2O_3–CeO_2$ system determined at 810 °C, $p_{O_2} = 100$ Pa using BaO starting material.

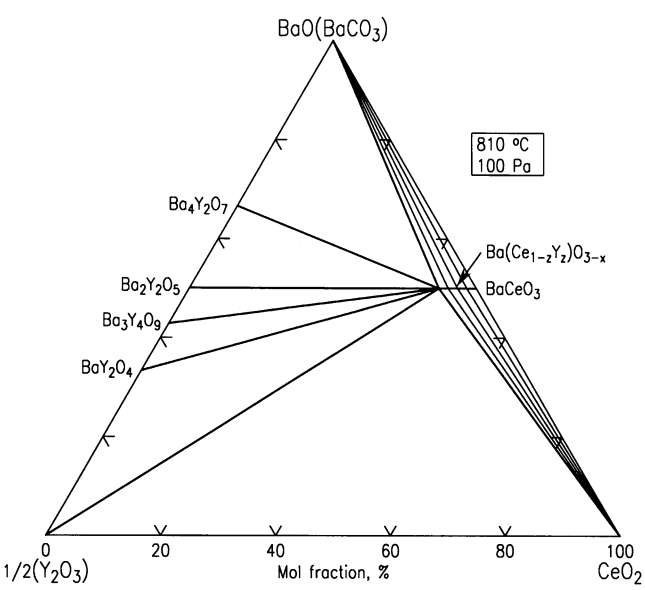

Fig. 4. Subsolidus diagram of the $BaO–Y_2O_3–CeO_2$ system determined at 810 °C, $p_{O_2} = 100$ Pa using $BaCO_3$ starting material.

There is no new ternary phase in this system except for the solid solution of the Y-doped $BaCeO_3$ phase, $Ba(Ce_{1-z}Y_z)O_{3-x}$. The range of this solid solution was determined to be rather small, namely, $0 \leqslant z \leqslant 0.13$. The extent of this solid solution depends on temperature and on oxygen partial pressure [56]. Extensive studies have been reported on the $Ba(Ce_{1-z}Y_z)O_{3-x}$ mixed conductors. These studies include diffusional creep [57], high temperature deformation studies [58], and transport properties for hydrogen separation [59]. We have studied the structure of a solid solution member using neutron diffraction (reported below), which has essentially a perovskite-related structure. Despite extensive solid solution formed at higher temperature (for example, 20.5 mole fraction % of yttria in ceria at 1500 °C in air), under ≈ 810 °C and $p_{O_2} = 100$ Pa, we found no significant solid solution of between Y_2O_3 and CeO_2.

(b) Crystal structure of $Ba(Ce_{1-z}Y_z)O_{3-x}$. The final neutron refinement residuals for one of the selected $Ba(Ce_{1-z}Y_z)O_{3-x}$ phases, $Ba(Ce_{0.94}Y_{0.06})O_{2.84}$, were found to be w_{R_p} of 0.0668 and $R_p = 0.0557$ for 2999 observed data. The goodness of fit (χ^2) value was determined to be 1.688 with 50 variables. Fig. 5 illustrates the Rietveld refinement results for $Ba(Ce_{0.94}Y_{0.06})O_{2.84}$ (as compared to the expected synthesized composition of $Ba(Ce_{0.95}Y_{0.05})O_{3-x}$). In this diagram, the upper graph shows the fit between the experimental and calculated patterns while the lower graph shows the difference between these two patterns.

The structure refinement results for $Ba(Ce_{0.94}Y_{0.06})O_{2.84}$ is shown in Table 4, which includes the atomic coordinates, isotropic displacement factors, and site symmetry of the cations. Table 5 gives the anisotropic displacement factors for oxygen atoms. The refinement results show that the O(5) site is only partially occupied. Y was found to substitute for the Ce site with an occupancy of 0.06(2), giving rise to the unit cell content of $Ba_4(Ce_{3.76}Y_{0.24})O_{11.36}$, or the chemical formula of $Ba(Ce_{0.94}Y_{0.06})O_{2.84}$, with $Z = 4$, (space group of *Pmcn*, $a = 8.7817(4)$ Å, $b = 6.2360(4)$ Å, and $c = 6.2190(3)$ Å, $V = 340.57$ Å^3, and a density 6.236 g/cm^3). As the sample was prepared under 0.1% O_2, the oxygen content was determined to be less than the value of 3.0. The charge balance calculation leads to the chemical formula of $Ba(Ce^{3+}{}_{0.26}Ce^{4+}{}_{0.68}Y_{0.06})O_{2.84}$.

Table 6 gives the relevant bond distances, bond angles and bond valence sum for the Ba site and for (Ce,Y) site. Figs. 6, 7 and 8 give the crystal structure of $Ba(Ce_{0.94}Y_{0.06})O_{3-x}$ viewing along *a*-, *b*-, and *c*-axis, respectively. This phase is essentially isostructural with the well-known perovskite phase, $BaCeO_3$. It consists of distorted corner-sharing CeO_6 octahedra. The $[CeO_6]$ octahedra all rotated around the *a*-, *b*- and *c*-axis. The *a*-axis rotation angle was found to be 10.30°. The corresponding tilting angles around the *c*-axis is 11.54°, while the rotation angle around the *b*-axis is very small, 1.24°. The Ba ions are located in the interstices (Fig. 7) and forms distorted 9-membered cages. The distorted ratio is 0.81. The distorted ratio (ratio of the shortest bond distance to longest one, with 1.0 being ideal) is 0.997.

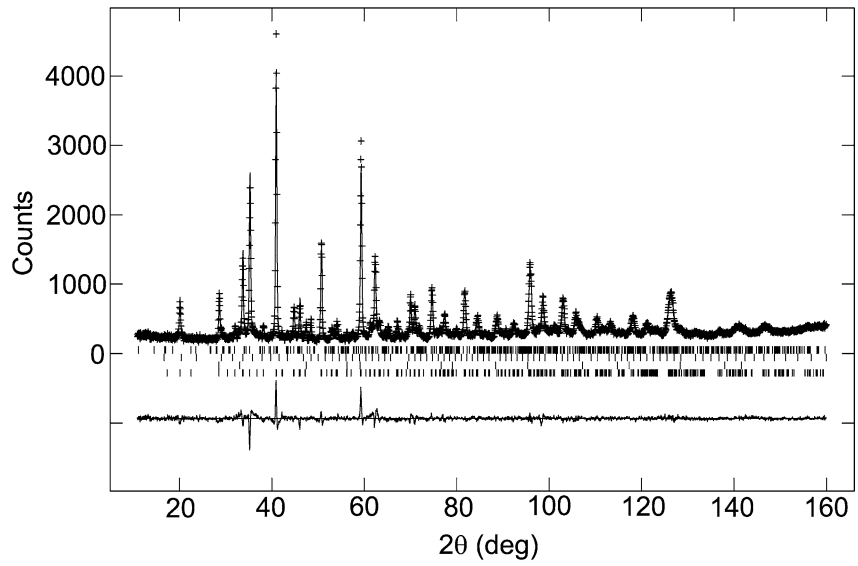

Fig. 5. Rietveld refinement results for $Ba(Ce_{0.94}Y_{0.06})O_{2.84}$. The upper graph shows the fit between the experimental and calculated patterns while the lower graph shows the difference between the two patterns.

Table 4
Atomic coordinates and displacement factors for $Ba(Ce_{0.94}Y_{0.06})O_{2.84}$

Atoms	x	y	z	U_{iso}	n	W
Ba	0.25	−0.0031(11)	0.0145(7)	1.23(9)	1.0	4 c
Ce	0	1/2	0	0.819(8)	0.94(2)	4 b
Y	0	1/2	0	0.819(8)	0.06(2)	4 b
O4	0.25	0.4281(7)	−0.0127(10)		1.0	4 c
O5	0.0378(3)	0.7245(6)	0.2752(5)		0.92(1)	8 d

Space group *Pmcn* (No. 62), $a = 8.7817(4)$ Å, $b = 6.2360(4)$ Å, $c = 6.2190(3)$ Å, $V = 340.57$ Å, $Z = 4$, and a density 6.236 g/cm^3; n = fraction of site occupancy; W is used to indicate number of positions and Wyckoff position.

Table 5
Displacement factors for O4 and O5 in $Ba(Ce_{0.94}Y_{0.06})O_{2.84}$

Atom	U_{11}	U_{22}	U_{33}	U_{12}	U_{13}	U_{23}
O4	0.47(19)	2.62(23)	3.06(31)	0	0	−0.33(22)
O5	1.56(15)	2.18(19)	1.10(17)	0.30(17)	−0.33(14)	−0.71(12)

Anisotropically refined atoms are given in the form of the isotropic equivalent displacement parameter defined as: $(4/3)\{a^2U_{11} + b^2U_{22} + c^2U_{33} + ab(\cos\gamma)U_{12} + ac(\cos\beta)U_{13} + bc(\cos\alpha)U_{23}\}$.

Figs. 6 to 8 show that the octahedra are rotated and tilted with respect to each other.

The bond valence sum (BVS) values [60,61] calculated for the Ba site is 1.598, which is substantially smaller than the ideal value of 2. Ba is therefore under a tensile strain or it is rattling inside a much larger cage. Because of the mixed valence of Ce^{3+}, Ce^{4+}, Y^{3+} at the Ce site, the BVS value at the Ce site was found to be 3.729, which is very close to the expected value of 3.68 (computed as a weighted sum of the fractional occupancy of (Ce^{3+}, Ce^{4+}, Y) in the formula $Ba(Ce^{3+}{}_{0.26}Ce^{4+}{}_{0.68}Y_{0.06})O_{2.84}$). Therefore, it appears that strain is relieved as a result of distortion, rotation and tilting of the $(Ce,Y)O_6$ octahedra.

Table 6
Selected bond lengths and bond angles in $Ba(Ce_{0.94}Y_{0.06})O_{3-x}$

Atoms	Bond distance (Å)		Atoms	Bond distance (Å)	
Ba–O1	2.694(9)		(Ce,Y)–O1	2.2422(9)	×2
Ba–O1	3.312(8)		(Ce,Y)–O2	2.236(4)	×2
Ba–O1	2.977(8)		(Ce,Y)–O2′	2.240(4)	×2
Ba–O2	2.998(6)	×2			
Ba–O2′	2.756(5)	×2	D.R.	0.997	
Ba–O2″	3.180(4)	×2	BVS	3.729/[3.68]	
D.R.	0.813				
BVS	1.598				

Distances printed are those < 3.6 Å. BVS is the bond valence calculated from the measured bond distances and from reference values given by Brese and O'Keeffe [60] and Brown and Altermatt [61] (2.29 Å for Ba–O, 2.014 Å for Y–O, 2.151 Å for Ce^{3+}, and 2.028 Å for Ce^{4+}). The BVS value for the Ce site is computed using both the bond valence value of Y–O, Ce^{3+}–O and Ce^{4+}–O weighted by the site occupancy. [BVS] is the expected valence value weighted by the site occupancy; D.R. is the distortion ratio (ratio of the shortest to the longest bond distance).

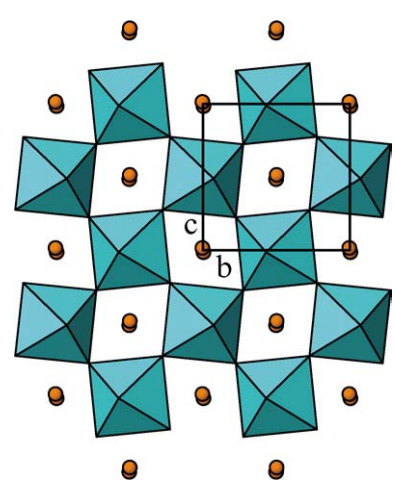

Fig. 6. Crystal structure of $Ba(Ce_{0.94}Y_{0.06})O_{2.84}$ viewing along a-axis.

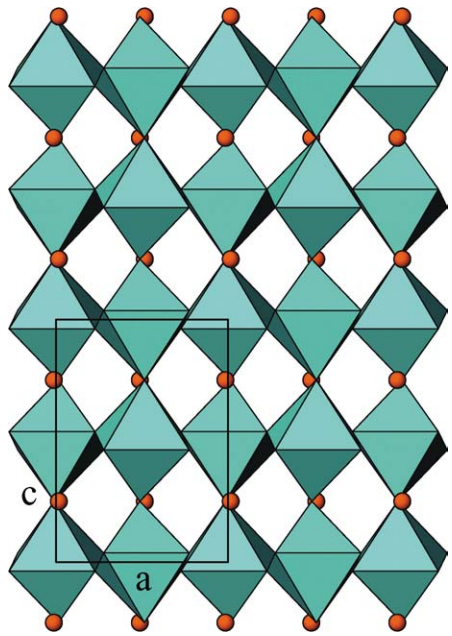

Fig. 7. Crystal structure of $Ba(Ce_{0.94}Y_{0.06})O_{2.84}$ viewing along *b*-axis.

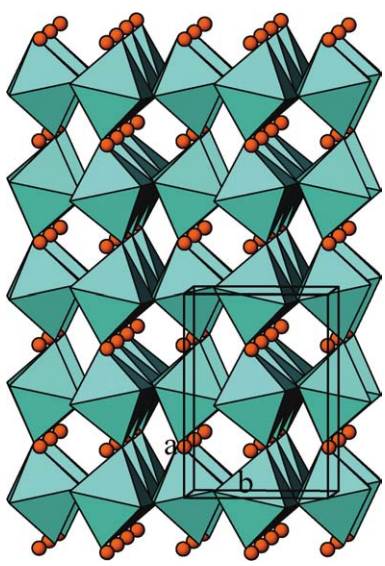

Fig. 8. Crystal structure of $Ba(Ce_{0.94}Y_{0.06})O_{2.84}$ viewing along *c*-axis.

(c) Reference powder diffraction patterns. Tables 7 and 8 give the reference patterns for $Ba(Y_{0.13}Ce_{0.87})O_{2.93}$ and $Ba(Y_{0.10}Ce_{0.90})O_{2.95}$. These reference patterns have been submitted to the International Centre for Diffraction Data (ICDD) to be included in the Powder Diffraction File [21]. In these tables, the symbols *M* and + refer to peaks containing contributions from two and more than two reflections, respectively. The symbol ∗ indicates the particular peak has the strongest intensity of the entire pattern and is designated a value of '999'. The intensity values reported are integrated intensities rather than peak heights.

CeO_2–Y_2O_3–CuO_x. Fig. 9 gives the phase diagram of the CeO_2–Y_2O_3–CuO_x system. At 810 °C under $p_{O_2} = 100$ Pa,

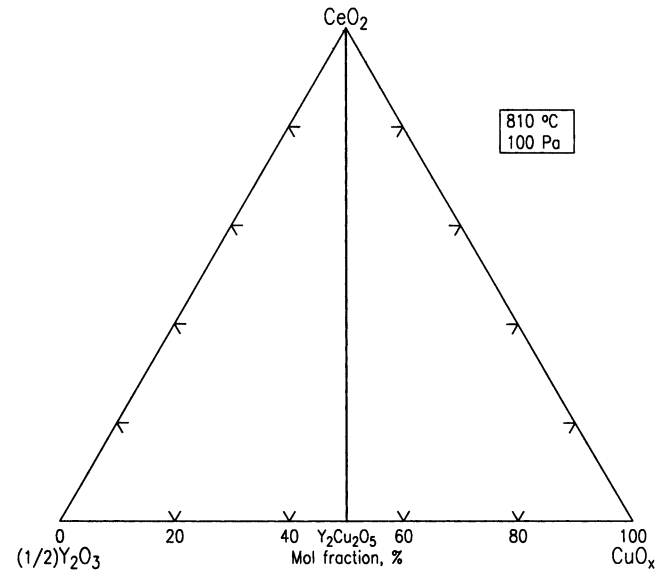

Fig. 9. Phase diagram of the CeO_2–Y_2O_3–CuO_x system determined at 810 °C and $p_{O_2} = 100$ Pa.

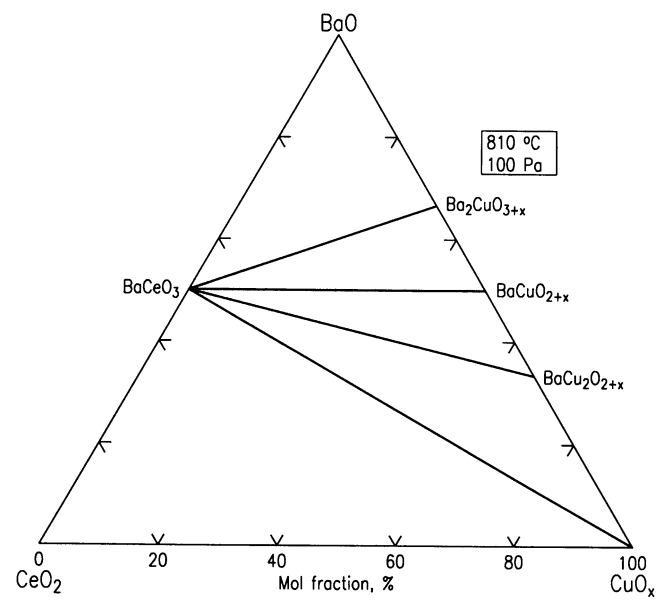

Fig. 10. Phase diagram of the BaO–CeO_2–CuO_x system determined at 810 °C and $p_{O_2} = 100$ Pa.

and at 930 °C under air, the CeO_2–Y_2O_3–CuO_x diagrams show only one tie-line from Y_2O_3 to $Y_2Cu_2O_5$. This phase is orthorhombic, *Pna2₁* (33), $a = 10.79$ Å, $b = 3.496$ Å, and $c = 12.456$ Å [62]. The phase $YCuO_2$ ($P6_3/mmc$, $a = 7.5206(1)$ Å, and $c = 11.410(1)$ Å [42]) which is the reduced version of $Y_2Cu_2O_5$ is not found in this system under $p_{O_2} = 100$ Pa.

BaO–CeO_2–CuO_x. The phase diagram of the ternary BaO–CeO_2–CuO_x system is shown in Fig. 10. No ternary phases was observed. This diagram bears no resemblance to any of the BaO–R_2O_3–CuO_x systems (R = lanthanides with a 3+ stable valence state) that were prepared under

Table 7
X-ray diffraction pattern of $Ba(Ce_{0.87}Y_{0.13})O_{2.93}$, space group *Pmcn*, $a = 8.7792(5)$ Å, $b = 6.2343(5)$ Å, $c = 6.2180(4)$ Å, $V = 340.32$ Å^3, $Z = 4$

d [Å]	*I*	*h*	*k*	*l*	*d* [Å]	*I*	*h*	*k*	*l*	*d* [Å]	*I*	*h*	*k*	*l*
4.40254	2	0	1	1	3.93543	5	1	1	1	3.11715	198	0	2	0
3.10858	999*	0	0	2M	3.10858	999*	2	1	1M	2.93066	20	1	0	2
2.54152	5	2	2	0	2.53710	4	2	0	2	2.20127	218	0	2	2
2.19480	105	4	0	0	1.79801	171	2	3	1	1.79433	334	4	2	0+
1.55857	29	0	4	0	1.55429	145	0	0	4M	1.55429	145	4	2	2M
1.39330	29	0	4	2	1.39157	88	2	3	3M	1.39157	88	0	2	4M
1.38852	64	6	1	1	1.27076	27	4	4	0	1.26855	25	4	0	4
1.17770	40	2	5	1	1.17630	38	4	4	2	1.17496	112	4	2	4+
1.17397	37	6	1	3	1.10063	17	0	4	4	1.09740	8	8	0	0
1.03905	6	0	6	0	1.03812	29	2	5	3	1.03692	26	2	3	5
1.03619	33	0	0	6M	1.03619	33	6	3	3M	1.03498	32	8	2	0M
1.03498	32	8	0	2M	0.98547	13	0	6	2	0.98372	38	4	4	4M
0.98372	38	0	2	6M	0.98212	26	8	2	2	0.93913	12	4	6	0
0.93816	25	6	5	1	0.93692	33	4	0	6M	0.93692	33	6	1	5
0.89901	28	4	6	2	0.89739	38	4	2	6M	0.89739	38	8	4	0M
0.89651	12	8	0	4	0.86436	29	2	7	1	0.86384	12	0	6	4
0.86306	65	0	4	6+	0.86218	81	6	3	5+	0.86159	29	8	2	4
0.86097	29	10	1	1										

The symbol '*d*' refers to *d*-spacing values, '*I*' refers to integrated intensity value (scaled according to the maximum value of 999; the symbol '*' indicates the strongest peak), the *h k l* values are the Miller indexes, M and + refer to peaks containing contributions from two and more than two reflections, respectively. The intensity values reported are integrated intensities rather than peak heights.

Table 8
X-ray diffraction pattern of $Ba(Ce_{0.90}Y_{0.10})O_{2.95}$, space group *Pmcn*, $a = 8.7795(4)$ Å, $b = 6.2364(3)$ Å, $c = 6.2165(3)$ Å, $V = 340.36$ Å^3, $Z = 4$

d [Å]	*I*	*h*	*k*	*l*	*d* [Å]	*I*	*h*	*k*	*l*	*d* [Å]	*I*	*h*	*k*	*l*
4.40272	3	0	1	1	3.93558	5	1	1	1	3.11818	199	0	2	0
3.10852	999*	2	1	1M	3.10852	999*	0	0	2M	2.93003	18	1	0	2
2.20136	220	0	2	2	2.19487	105	4	0	0	1.91890	5	1	1	3
1.79843	174	2	3	1	1.79422	336	2	1	3+	1.55909	29	0	4	0
1.55426	147	4	2	2M	1.55426	147	0	0	4M	1.39360	29	0	4	2
1.39156	92	2	3	3M	1.39156	92	0	2	4M	1.38857	65	6	1	1
1.27105	27	4	4	0	1.26836	26	4	0	4	1.17804	41	2	5	1
1.17649	38	4	4	2	1.17490	112	4	2	4+	1.17391	37	6	1	3
1.10068	18	0	4	4	1.09743	8	8	0	0	1.03830	29	2	5	3
1.03683	26	2	3	5	1.03618	33	6	3	3M	1.03618	33	0	0	6M
1.03501	32	8	2	0M	1.03501	32	8	0	2M	0.98574	13	0	6	2
0.98390	26	4	4	4	0.98322	12	0	2	6	0.98215	26	8	2	2
0.93939	12	4	6	0	0.93834	27	6	5	1	0.93678	34	4	0	6M
0.93678	34	6	1	5M	0.89922	28	4	6	2	0.89734	39	4	2	6
0.89646	12	8	0	4	0.86462	31	2	7	1	0.86398	12	0	6	4
0.86311	67	6	5	3+	0.86214	81	6	3	5+	0.86156	30	8	2	4
0.86100	29	10	1	1										

The symbol '*d*' refers to *d*-spacing values, '*I*' refers to integrated intensity value (scaled according to the maximum value of 999; the symbol '*' indicates the strongest peak), the *h k l* values are the Miller indexes, M and + refer to peaks containing contributions from two and more than two reflections, respectively. The intensity values reported are integrated intensities rather than peak heights.

the same experimental conditions [33,37,38]. Apparently the Ce^{2+} and Ce^{4+} oxidation states have played an important role in the crystal chemistry of this system. Four tie-lines were found to originate from $BaCeO_3$ to the four phases in the BaO–CuO_x binary system, namely, Ba_2CuO_{3+x}, $BaCuO_{2+x}$, $BaCu_2O_{2+x}$ and CuO_x. The $Ba_2CeCu_3O_x$ phase reported in literature [63] was not observed here under the reduced condition. According to Gao et al., this phase is stable under oxygen, with a tentative space group of *Pmmm*, $a = 6.028$ Å, $b = 6.232$ Å, and $c = 8.779$ Å. A possible structure model is reported to be based on the superlattice of the cubic $BaCeO_3$ phase [64].

BaO–Y_2O_3–CuO_x. The phase diagram (Fig. 11) of this system has already been published [33] from this laboratory. In summary, this is the system consists of the high T_c Y-213 phase. There are a total of 4 ternary oxide phases, namely, $Ba_4YCu_3O_x$, $Ba_6YCu_3O_x$, BaY_2CuO_5, and the superconductor phase $Ba_2YCu_3O_{6+x}$. The $Ba_2YCu_3O_{6+x}$ phase was found to be compatible with the $Ba_4YCu_3O_x$ phase, whereas the literature reports indicate a tie-line between $BaCuO_{2+x}$ and BaY_2CuO_5 [58,59]. Since the majority of the literature data were not conducted entirely under atmospherically controlled conditions, it is clear that the presence of CO_2 affects the tie-line relationships. For applications of phase equilibria

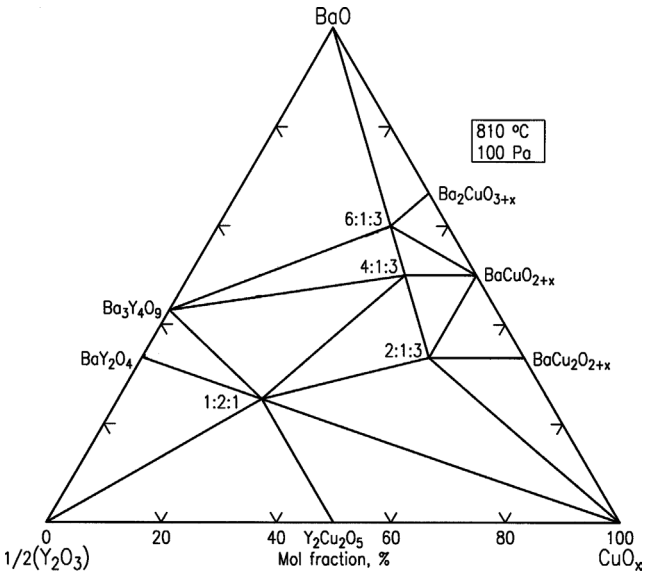

Fig. 11. Phase diagram of the $BaO–Y_2O_3–CuO_x$ system determined at 810 °C and $p_{O_2} = 100$ Pa [33].

to coated-conductor processing, phase diagrams constructed under carbonate-free conditions should be employed.

4. Summary

Phase equilibria of the $BaO–Y_2O_3–CeO_2–CuO_x$ system was studied along the nonbinary $Ba_2YCu_3O_{6+x}–CeO_2$ join in order to understand the interaction between the $Ba_2YCu_3O_{6+x}$ superconductor film and the buffer CeO_2 layer of coated conductor materials. Two four-phase regions were identified that gives rise to a total of five possible phases to appear at the $Ba_2YCu_3O_{6+x}–CeO_2$ interface. The occurrence of these reactants depends on the relative composition of $Ba_2YCu_3O_{6+x}$ and CeO_2. These phases are: $Ba_2YCu_3O_{6+x}$, $Ba(Ce_{1-z}Y_z)O_{3-x}$, BaY_2CuO_5, Cu_2O and CeO_2. The lowest melting temperature of the system was determined to be ≈ 860 °C, which is significantly higher than the processing temperature of the RABiTS/film system. Phase diagrams of the subsystems $BaO–Y_2O_3–CeO_2$, $CeO_2–Y_2O_3–CuO_x$ and $BaO–CeO_2–CuO_x$ prepared under 100 Pa p_{O_2} and 810 °C were also reported. The crystal structure of $Ba(Ce_{0.94}Y_{0.06})O_{3-x}$ was studied by neutron diffraction. Work will continue to characterize the interaction of $Ba_2YCu_3O_{6+x}$ with other important buffer materials, such as $SrTiO_3$ and Gd_3NbO_7.

Acknowledgements

This project was partially supported by the U.S. Department of Energy. Nils Swanson and Dr. Peter Schenck of NIST are thanked for their graphical assistance. We also acknowledge the valuable contributions from our colleagues, Drs. A. Goyal, M. Paranthaman, and R. Feenstra from Oak Ridge National laboratory, and Dr. T. Holesinger from Los Alamos Laboratory.

References

[1] S.R. Foltyn, E.J. Peterson, J.Y. Coulter, P.N. Arendt, Q.X. Jia, P.C. Dowden, M.P. Maley, X.D. Wu, D.E. Peterson, J. Mater. Res. 12 (1997) 2941–2946.
[2] Y. Iijima, M. Hosaka, N. Tanabe, N. Sadakata, T. Saitoh, O. Kohno, K. Takeda, J. Mater. Res. 12 (1997) 2913–2923.
[3] A.P. Malozemoff, S. Annavarapu, L. Fritzemeier, Q. Li, V. Prunier, M. Rupich, C. Thieme, W. Zhang, A. Goyal, M. Paranthaman, D.F. Lee, Supercond. Sci. Technol. 13 (2002) 473–476.
[4] M. Paranthaman, C. Park, X. Cui, A. Goyal, D.F. Lee, P.M. Martin, T.G. Chirayil, D.T. Verebelyi, D.P. Norton, D.K. Christen, D.M. Kroeger, J. Mater. Res. 15 (12) (2000) 2647–2652.
[5] A. Goyal, D.F. Lee, F.A. List, E.D. Specht, R. Feenstra, M. Paranthaman, X. Cui, S.W. Lu, P.M. Martin, D.M. Kroeger, D.K. Christen, Kang, D.P. Norton, C. Park, D.T. Verebelyi, J.R. Thompso, R.K. Williams, T. Aytug, C. Cantoi, Physica C 357 (2001) 903–913.
[6] T. Aytug, A. Goyal, N. Rutter, M. Paranthaman, J.R. Thompson, H.Y. Zhai, D.K. Christen, J. Mater. Res. 18 (4) (2003) 872–877.
[7] M. Paranthaman, A. Goyal, F.A. List, E.D. Specht, D.F. Lee, P.M. Martin, Q. He, D.K. Christen, D.P. Norton, J.D. Budai, D.M. Kroeger, Physica C 275 (1997) 266–272.
[8] U. Balachandran, Practical superconductivity development for electrical power applications, Argonne National Laboratory, Annual Report for FY 2001, ANL-02/03.
[9] U. Balachandran, Practical superconductivity development for electrical power applications, Argonne National Laboratory, Quarterly Report for January–March 2002.
[10] J.O. Willis, R.D. Ray II, T.G. Holesinger, R. Zhou, K.V. Salazar, J.Y. Coulter, J.J. Gingert, D.S. Phillips, D.E. Peterson, in: Proceedings of the 7th US/Japan Workshop on High Temperature Superconductors, Tsukuba, Japan, 22–24 October 1995.
[11] U. Balachandran, in: W. Wong-Ng, U. Balachandran, A.S. Bhalla (Eds.), Impact of Recent Advances in Synthesis and Processing of Ceramic Superconductors, in: Ceramic Transactions, vol. 84, Amer. Ceram. Soc., 1998, p. 157.
[12] U. Balachandran, A.N. Iyer, P. Haldar, J.G. Hoehn Jr., L.R. Motowidlo, in: K. Kristen, C. Burnham (Eds.), Proceedings of The Fourth International conference ad Exhibition: World Congress on Superconductivity, vol. II, Orlando, FL, June 27 – July 1, 1994, pp. 639–649.
[13] D.Y. Kaufman, M.T. Lanagan, S.E. Dorris, J.T. Dawley, I.D. Bloom, M.C. Hash, N. Chen, M.R. DeGuire, R.B. Poeppel, Appl. Supercond. 1 (1–2) (1993) 81–91.
[14] K. Sato, V. Hikata, H. Mukai, M. Ueyama, N. Shibata, T. Kato, T. Masuda, M. Nagata, K. Iwata, T. Mitsui, IEEE Trans. Mag. 27 (1991) 1231–1238.
[15] M. Rupich, American Superconductor Corp., private communication.
[16] L. Wu, Y. Zhu, V.F. Solovyov, H.J. Wiesmann, A.R. Moodenbaugh, R.L. Sabatini, M. Suenaga, J. Mater. Res. 16 (10) (2001) 2869–2884.
[17] T.G. Holesinger, B.J. Gibbons, J.Y. Coulter, S.R. Foltyn, J.R. Groves, P.N. Arendt, in: M.P. Paranthaman, M.W. Rupich, K. Salama, J. Mannhart, T. Hasegawa (Eds.), Materials Research Society Symposium Proceedings 689, Materials for High-Temperature Superconductor Technologies. Symposium held November 26–29, 2001, Boston, MA, 2002, pp. 329–336.
[18] C.N.L. Edvardsson, U. Helmersson, L.D. Madsen, Z. Czigany, L. Ryen, E. Olsson, Physica C 304 (1998) 245–254.
[19] W.P.T. Derks, H.A.M. van Hal, C. Langereis, Physica C 156 (1988) 62–64.
[20] W. Wong-Ng, L.P. Cook, in: K.M. Nair, U. Balachandran, Y.-M. Chiang, A. Bhalla (Eds.), Ceramic Transaction, 18, Superconductivity in Ceramic Superconductors 2, Am. Ceram. Soc., Westerville, OH, 1991, p. 73.

[21] PDF, Powder Diffraction File, produced by ICDD, Newtown Square, 12 Campus Blvd., Newtown Squares, PA 19073-3273.
[22] H.M. Rietveld, J. Appl. Cryst. 2 (1969) 65–71.
[23] A.C. Larson, R.B. von Dreele, GSAS-General Structure Analysis System, US Government contract (W-7405-ENG-36) by the Los Alamos National laboratory, which is operated by the University of California for the U.S. Department of Energy, 1992.
[24] R.A. Young, The Rietveld Method, International Union of Crystallography Monograph, Oxford Scientific Publications, 1995.
[25] J. Ritter, Powd. Diffr. 3 (1988) 30–31.
[26] M.W. Chase Jr., NIST–JANAF Thermochemical Tables, fourth ed., J. Phys. Chem. Ref. Data, Monograph No. 9, 1998, p. 1952.
[27] R.J. Panlener, R.N. Blumenthal, AEC Report C00-1441-18 (1972).
[28] K. Kitayama, K. Nojiri, T. Sugihara, T. Katsura, J. Solid State Chem. 56 (1) (1985) 1–11.
[29] M. Ricken, J. Noelting, I. Riess, J. Solid State Chem. 54 (1) (1984) 89–99.
[30] I. Riess, Rieeeken, J. Noelting, Solid State Ionics 18–19 (2) (1986) 725–726.
[31] R. Koerner, J. Ricken, J. Noelting, I. Riess, J. Solid State Chem. 78 (1) (1989) 136–147.
[32] W. Wong-Ng, L.P. Cook, J. Res. Natl. Inst. Stand. Technol. 103 (1998) 379–403.
[33] W. Wong-Ng, L.P. Cook, J. Suh, Physica C 377 (2002) 107–113.
[34] J.P. Guha, D. Kolar, J. Mater. Sci. 6 (9) (1971) 1174–1177.
[35] C.N. Pieczulewski, K.S. Kirkpatrick, T.O. Mason, J. Am. Ceram. Soc. 73 (7) (1990) 2141–2143.
[36] W. Wong-Ng, L.P. Cook, Powder Diffr. 9 (4) (1994) 280.
[37] W. Wong-Ng, L.P. Cook, J. Suh, R. Coutts, J.K. Stalick, I. Levin, Q. Huang, J. Solid State Chem. 173 (2003) 476–488.
[38] W. Wong-Ng, L.P. Cook, J. Suh, J.A. Kaduk, Physica C 405 (2004) 47–58.
[39] Z.Y. Qiao, J.K. Liang, G.G. Rao, Beijing Keji DaxueXue-bao 13 (2) (1991) 154–161.
[40] A.J.S. Machado, R.F. Jardim, Mater. Lett. 19 (3–4) (1994) 177–183.
[41] I. Horsak, J. Sestak, B. Stepanck, Thermochim. Acta 234 (1–2) (1994) 233–243.
[42] T. Ishiguro, N. Ishizawa, N. Mitzutani, M. Kato, J. Solid State Chem. 49 (1983) 232–236.
[43] B.U. Kohler, M. Jansen, Z. Anorg. Allg. Chem. 543 (1986) 73–80.
[44] G.M. Kale, K.T. Jacob, Solid State Ionics 34 (4) (1989) 247–252.
[45] W. Zhang, K. Osamura, Mater. Trans., JIM 32 (11) (1991) 1048–1052.
[46] I. Horsak, J. Sestak, B. Stepanek, Thermochim Acta 234 (1–2) (1994) 233–243.
[47] K.N. Marushkin, G.D. Nipan, V.B. Lazarev, J. Chem. Thermodyn. 27 (5) (1995) 465–474.
[48] D.Y. Wang, D.S. Park, J. Griffith, A.S. Nowick, Solid State Ionics 2 (1981) 95–105.
[49] G.B. Balazs, R.S. Glass, Solid State Ionics 76 (1995) 155.
[50] V. Longo, L. Podda, J. Mater. Sci. 16 (3) (1981) 839.
[51] S.G. Yusupova, L.G. Bochkareva, M.G. Degen, I.A. Drozdova, V.G. Blushkova, V.A. Sadovnikov, Izv. Akadem. Nauk SSSR, Neorg. Mater. 27 (8) (1991) 1660–1664.
[52] N. Gabbitas, J.G. Thompson, R.L. Withers, A.D. Rae, J. Solid State Chem. 115 (1995) 23–36.
[53] C. Tian, S.W. Chan, Solid State Ionics 134 (2000) 89–102.
[54] W. Wong-Ng, B. Paretzkin, Powder Diffr. 6 (4) (1991) 187.
[55] Hk. Muller-Buschbaum, O. Schrandt, J. Alloys and Comp. 191 (1993) 151–154.
[56] K. Takeuchi, C.-K. Loong, J.W. Richardson Jr., J. Guan, S.E. Dorris, U. Balachandran, Solid State Ionics 138 (2000) 63–77.
[57] K.C. Goretta, E.T. Park, J. Guan, U. Balachandra, S.E. Dorris, J.L. Routbort, Solid State Ionics 111 (1998) 295–299.
[58] E.T. Park, K.C. Goretta, A.R. de Arellano-López, J. Guan, U. Balachandran, S.E. Dorris, J.L. Routbort, Solid State Ionics 117 (1999) 323–330.
[59] J. Guan, S.E. Dorris, U. Balachandran, M. Liu, Solid State Ionics 100 (1997) 45–52.
[60] N.E. Brese, M. O'Keeffe, Bond-valence parameters for solids, Acta Crystallogr. B 47 (1991) 192.
[61] I.D. Brown, D. Altermatt, Acta Crystallogr. B 41 (1985) 244–247.
[62] H.R. Freund, Hk. Müller-Buschbaum, Z. Naturforsch. B 32 (1997) 609–611.
[63] C. Gao, H. Wang, T. Cheng, Y. Liu, W. Liu, Y. Qian, Z. Chen, Solid State Comm. 70 (6) (1989) 631.
[64] K.S. Knight, Solid State Ionics 74 (1994) 109.